

# All-optical generation of surface plasmons in graphene

T. J. Constant,<sup>1,\*</sup> S. M. Hornett,<sup>1</sup> D. E. Chang,<sup>2,†</sup> and E. Hendry<sup>1</sup>

<sup>1</sup>*Electromagnetic Materials Group, Department of Physics,  
College of Engineering, Mathematics and Physical Sciences,  
University of Exeter, Exeter, Devon, UK. EX4 4QL.*

<sup>2</sup>*ICFO - Institut de Ciències Fotòniques,  
Mediterranean Technology Park, 08860 Castelldefels (Barcelona), Spain*

(Dated: October 2, 2015)

## Reducing Pump Fluence

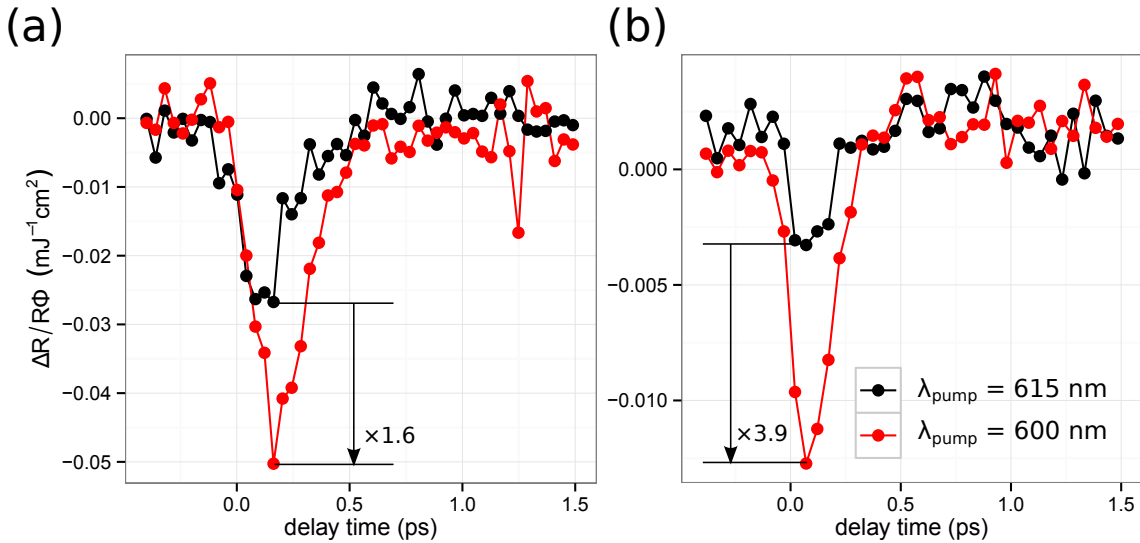


FIG. S1: Differential reflection normalized to pump fluence as a function of temporal overlap of the pulses for: (a) high-fluence pump and low-fluence probe, and (b) comparable fluence in both pump and probe. The black lines indicate the case for the difference frequency of 0 THz (no resonant plasmon coupling) and the red lines are for a difference frequency of 12 THz (resonant plasmon coupling).  $\theta_{\text{pump}} = 55^\circ$ ,  $\theta_{\text{probe}} = 70^\circ$ ,  $\lambda_{\text{probe}} = 615 \text{ nm}$ .

Since electron heating clearly has a negative impact in the experiment, one wants to minimize the pump intensity. However, reducing the light intensity also reduces our difference frequency coupling efficiency, since surface plasmon generation here is a nonlinear process. However, a possible route to better isolating coherent signals is to reduce the pump beam intensity and increase the probe beam intensity, illuminating the sample with similar fluences for both beams. This reduces the Pauli blocking of the probe induced by the pump beam, decreasing the signal due to saturable absorption decreases, while maintaining the efficiency of the difference frequency mixing process.

Figures S1(a) and S1(b) show differential reflection normalized to pump fluence for two difference frequencies, 0 THz ( $\lambda_{\text{pump}} = 615 \text{ nm}$ ) and 12 THz ( $\lambda_{\text{pump}} = 600 \text{ nm}$ ), measured for the angles  $\theta_{\text{pump}} = 50^\circ$  and  $\theta_{\text{probe}} = 70^\circ$ . In this geometry we expect a resonant enhancement for a difference frequency  $\sim 12$  THz due to plasmon excitation and no enhancement for 0 THz, as previously measured in fig. 3(b). In figure S1 (a) we show a typical measurement

for a high-power pump beam ( $0.26 \text{ mJ/cm}^2$ ) and a low power-probe beam ( $0.0028 \text{ mJ/cm}^2$ ). In this case, when the difference frequency matches that of the surface plasmon, a resonant change to the reflectivity by a factor of 1.6 occurs. For equal pump and probe fluences ( $\sim 0.07 \text{ mJ/cm}^2$ ), as shown in fig. S1(b), we observe a significant suppression of the background, non-resonant signal. The enhancement then measured from a non-resonant condition to the resonant surface plasmon excitation is increased to a factor of 3.9.

We also note that in the low-power pump case (fig. S1(b)), the lineshape of the recorded temporal dynamics is far more symmetric than in the high-power case (fig. S1(a)), which clearly exhibits the typical asymmetric lineshape indicative of incoherent carrier cooling dynamics.

### Increasing Pump Fluence

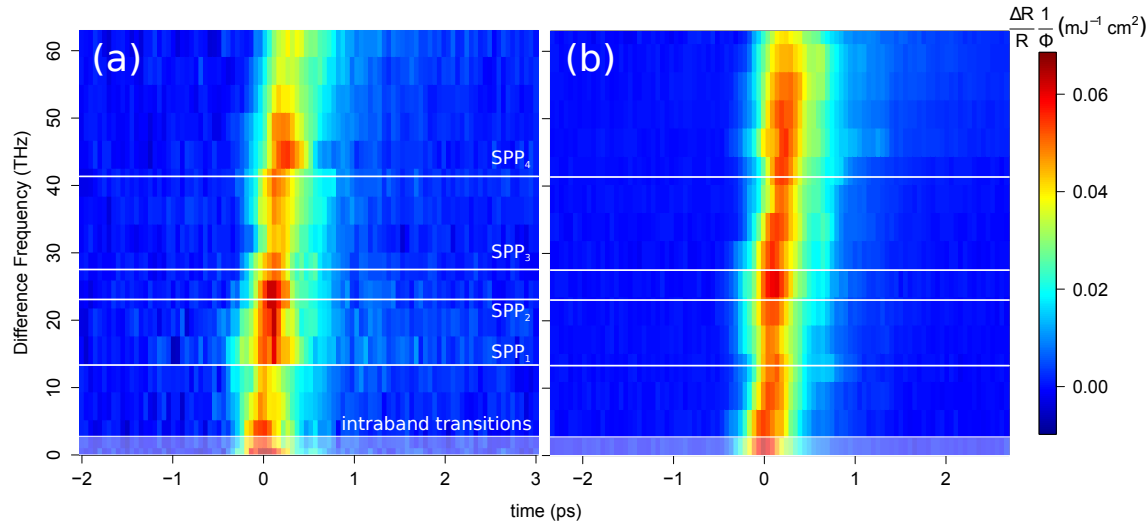


FIG. S2: Differential reflection normalized to fluence as a function of temporal overlap for: low (left) and high (right) pump fluence at  $\theta_{pump} = 15^\circ$  and  $\theta_{probe} = 125^\circ$ .

For pulsed fluence  $\sim 0.1 \text{ mJ/cm}^2$  we expect to generate an electron temperature of  $\sim 1000 \text{ K}$ [S1]. This means that we are probing a very non-equilibrium electron distribution. In order to investigate the effect of this electron heating, we increased the pump fluence used in the experiment to  $\sim 1.1 \text{ mJ/cm}^2$ . These results are shown in fig. S2. We find that a higher fluence significantly suppresses the surface plasmon resonance features with

respect to the background, off-resonance signal. We believe two factors contribute to this effect: firstly, an increased electron temperature will increase saturable absorption, the effect primarily responsible for the incoherent background signal. Secondly, due to the negative photoconductivity usually exhibited by graphene for pulsed femtosecond excitation[S2], one can expect increased losses and quenching of the surface plasmon, leading to broadening of the spectral features associated with their excitation.

Evidence that the increased electron temperature also raises the effective Fermi energy of the sample can be inferred by comparing fig. S2(a) and fig. S2(b), where the resonant regions of differential reflectivity shift to higher frequencies in the high-fluence case, as would be expected for the graphene surface plasmon dispersion for a higher doping level.

### Polarization Dependence

The experiment shown in fig. 3(c) was repeated with the pump and probe both polarized with the electric vector parallel to the graphene surface (transverse electric, TE polarized). Under these circumstances we expect surface plasmon excitation to be suppressed. The

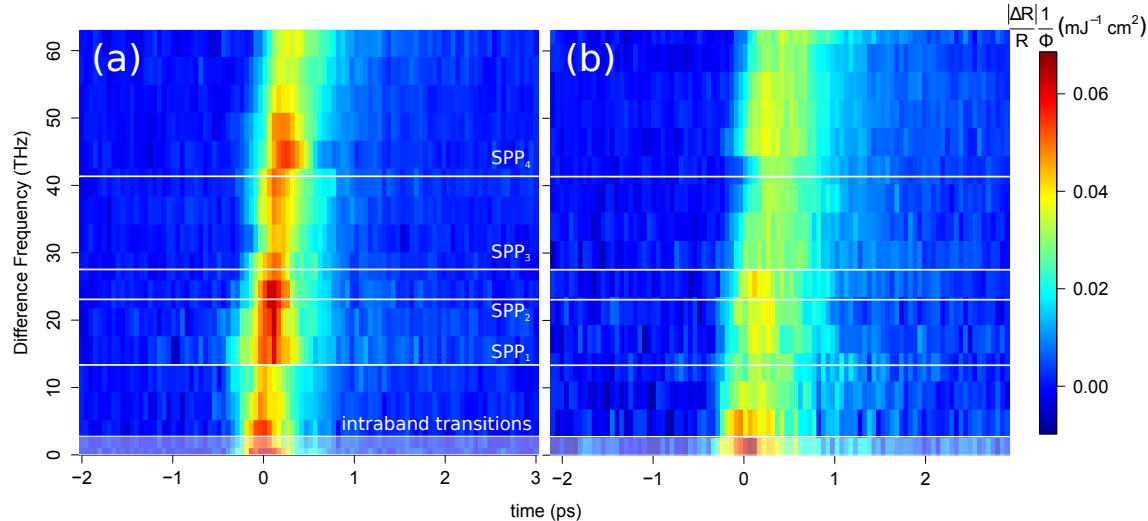


FIG. S3: Differential reflection normalized to pump fluence as a function of temporal overlap for transverse magnetic (a) and transverse electric (b) polarizations. The resonances for the predicted surface plasmon frequencies are clearly suppressed (labelled), while the intraband resonance is largely unaffected.

results are shown in figure S3. When illuminating with TE polarized light, there is a clear decrease in the nonlinear enhancement to the reflectivity for the 23-27 THz peak and the  $\sim 45$  THz peak. The peak at  $\sim 0$  THz is of the same order in both polarization cases, suggesting that the nonlinearity arising due to the intraband transitions are less sensitive to the polarization of the light. This is attributed to how carriers respond to the EM field in the plane of the surface. Since, for the intraband response the conductivity functions are in-plane, they make no distinction as to the out of plane component (which distinguishes TE and TM polarization).

While the higher-frequency resonances are strongly suppressed, they are not absent completely: we attribute this to imperfect polarization of the beams and inhomogeneity in the graphene sample.

### Higher Difference Frequencies

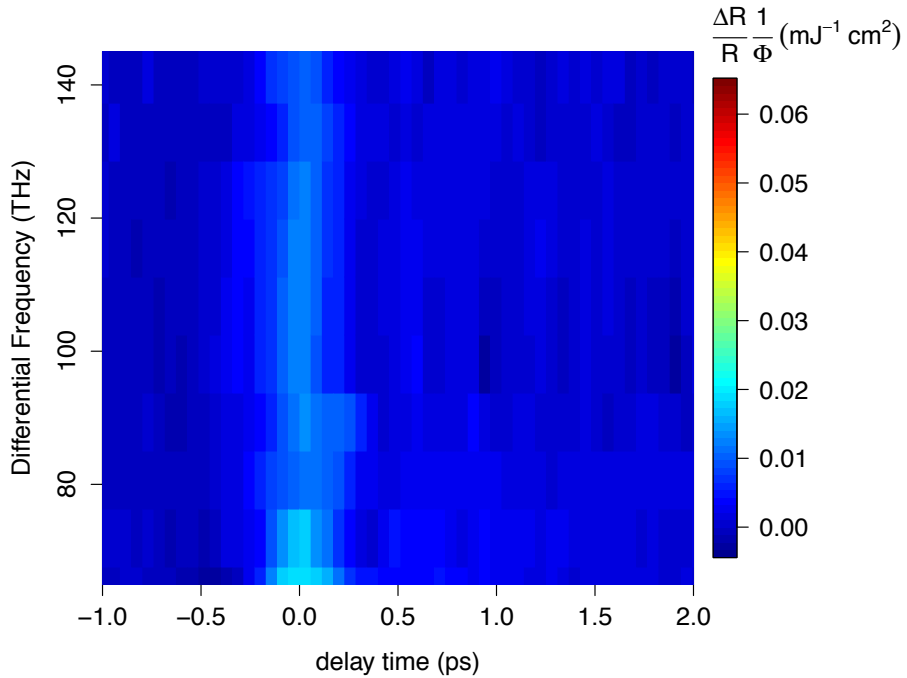


FIG. S4: Plot of differential reflection normalized to pump fluence as a function of temporal overlap for  $\theta_{pump} = 15^\circ$  and  $\theta_{probe} = 125^\circ$  at higher frequencies. The colorscale has been scaled to fig. 3(c) for ease of comparison.

We have preformed several measurements for a wider range of difference frequencies. In figure S4, we present measurements taken for  $\theta_{pump} = 15^\circ$  and  $\theta_{probe} = 125^\circ$ , where the pump wavelength was varied from 540 nm to 475 nm, with the probe wavelength fixed at 615 nm. This gives a difference frequency range from 70 THz to 140 THz. For these larger difference frequencies, we observe no resonance features above 70 THz, indicating there is no coherent coupling to higher frequency modes.

### Theoretical Model

We describe a theoretical model of two continuous-wave, free-space beams of frequencies  $\omega_{1,2}$  (without loss of generality, assume that  $\omega_1 > \omega_2$ ) interacting with graphene via a difference frequency generation process. The convention in our calculations to define the field polarizations and beam angles is illustrated in Fig. S6. The beams are taken to be incident from air (refractive index  $n \approx 1$ ). Important to modeling this experiment is the inclusion of a frequency-dependent and complex refractive index of the substrate at low frequencies, in order to capture the lattice vibrations in silica and the resulting surface optical phonons. To do this, we take a simple dielectric response model based upon three transverse optical (TO) phonon modes [S3],

$$n^2(\omega) = \epsilon_\infty + \sum_{j=1}^3 \frac{f_j \omega_{TO,j}^2}{\omega_{TO,j}^2 - \omega^2 - i\omega\gamma_{TO,j}}. \quad (\text{S1})$$

From Ref. [S3], the high-frequency dielectric constant is taken to be  $\epsilon_\infty = 2.4$ , while the TO phonon frequencies and oscillator weights are  $\omega_{TO} = 2\pi \times (13.44, 23.75, 33.84)$  THz and  $f = (0.7514, 0.1503, 0.6011)$ , respectively. The damping rates are taken to be  $\gamma_{TO} = 2\pi \times (0.80, 1.27, 1.27)$  THz. The resulting real and imaginary parts of the refractive index, plotted in Fig. S5, approximately correspond to experimentally measured values [S4]. In practice, this refractive index function is only relevant for the substrate response at the low difference frequency of  $\omega_3 = \omega_1 - \omega_2$ , while for the high frequencies  $\omega_{1,2}$  the response is nearly frequency-independent,  $n \approx \sqrt{\epsilon_\infty}$ .

In general, one can obtain equations relating the reflection and transmission coefficients to each other by enforcing electromagnetic boundary conditions (continuity of the normal electric displacement and tangential electric field) at the graphene interface. The solution

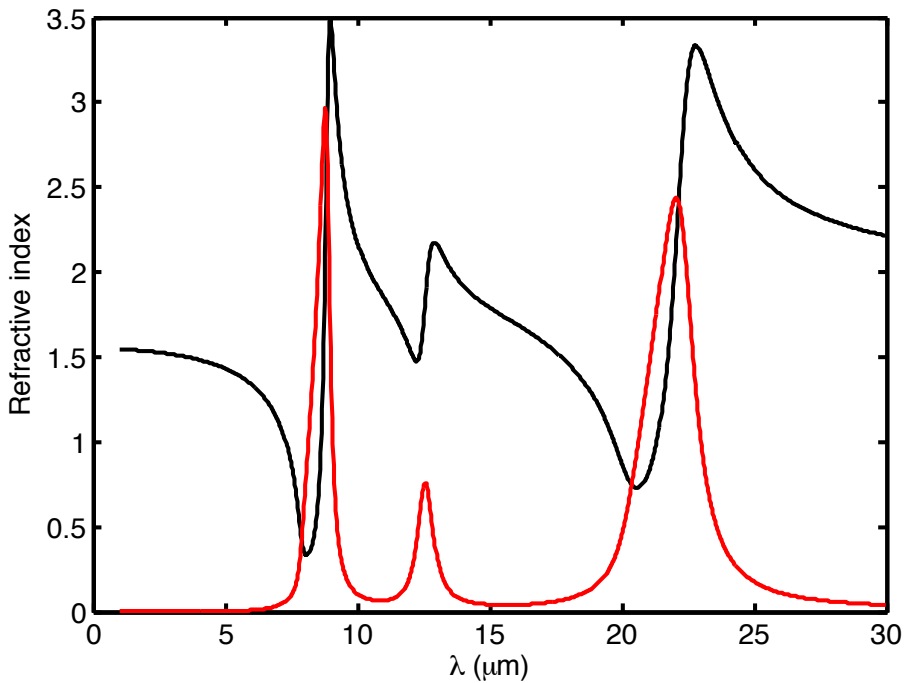


FIG. S5: Real (black) and imaginary (red) parts of the refractive index of silica versus free-space wavelength ( $\lambda = 2\pi c/\omega$ ), based upon the model of Eq. (S1).

for the transmission coefficient of field  $i$  ( $i = 1, 2$ ) is readily found to be

$$t_i = \frac{2 \sin \theta_i}{n_i \sin \theta_i + \sin \phi_i} - \frac{(\rho_{is}/\epsilon_0) \sec \phi_i \sin \theta_i}{E_{Ii}(n_i^2 \sin \theta_i + n_i \sin \phi_i)}, \quad (\text{S2})$$

where  $n_i = n(\omega_i)$  denotes the substrate refractive index at the field frequency, while the reflection coefficient is related by  $r_i = 1 - t_i \sin \phi_i \csc \theta_i$ . Here  $E_{Ii}$  are the incident field amplitudes, and  $\theta_i$  and  $\phi_i$  are the angles of the fields on the vacuum and substrate sides, respectively.  $\rho_{is} = \rho(\omega_i, k_{ix})$  is the graphene surface charge density at frequency  $\omega_i$  and in-plane wavevector  $k_{ix} = (\omega_i/c) \cos \theta_i$ . Note that the first term on the right-hand side of Eq. (S2) reproduces the standard Fresnel coefficient in the absence of a graphene layer ( $\rho_{is} = 0$ ). The angle of the transmitted field is related to the incident by Snell's Law,  $\cos \theta_i = n_i \cos \phi_i$ .

The surface charge density can be related to the current density  $J$  in the graphene layer via the continuity equation, which in the Fourier domain reads

$$\rho_s(\omega, k_x) = (k_x/\omega) J_x(\omega, k_x). \quad (\text{S3})$$

At the same time, the current density can be related to the electric fields via conductivity

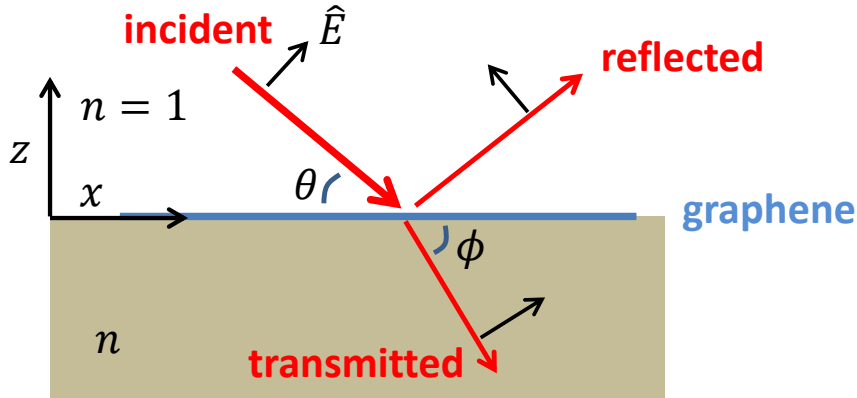


FIG. S6: Illustration of  $p$ -polarized electromagnetic fields propagating in the  $x$ - $z$  plane and interacting with graphene. The fields  $i = 1, 2$  consist of incident, reflected, and transmitted components, with the directions of propagation and polarizations indicated by the red and black arrows, respectively. The angles of incidence and transmission are  $\theta$  and  $\phi$ . The incident field is assumed to propagate in vacuum (refractive index  $n = 1$ ), while the graphene sits on top of a substrate with index  $n$  (possibly frequency dependent).

functions. We are particularly interested in the case of difference frequency generation, where the field produced at the difference frequency and wavevector  $\omega_3 = \omega_1 - \omega_2$  and  $k_{3x} = k_{1x} - k_{2x}$  is resonantly enhanced by aligning them with the plasmon dispersion of graphene  $\omega_p(k_x)$ . This motivates a truncated model in which we include only the linear and second-order conductivities, and frequencies  $\omega_{1,2}$  and  $\omega_3$  (thus left out is sum frequency generation and the generation of even higher harmonics). Then, the current density for field 1 is given by

$$J_x(\omega_1, k_{1x}) = \sigma^{(1)}(\omega_1, k_{1x})E_x(\omega_1, k_{1x}) + \sigma^{(2)}(\omega_1, k_{1x}; \omega_2, k_{2x}, \omega_3, k_{3x})E_x(\omega_2, k_{2x})E_x(\omega_3, k_{3x}). \quad (\text{S4})$$

Here,  $E_x(\omega_1, k_{1x}) = t_1 E_{1I} \sin \phi_1$  is the total parallel field for  $i = 1$  at the graphene layer, which we have written in terms of the incident field and transmission coefficient.  $\sigma^{(1)}$  is the linear conductivity function, while  $\sigma^{(2)}(\omega_1, k_{1x}; \omega_2, k_{2x}, \omega_3, k_{3x})$  is the second-order nonlinear conductivity functions relating the current density generated at  $\omega_1, k_{1x}$  given fields at  $\omega_2, k_{2x}$  and  $\omega_3, k_{3x}$ . Similar expressions as Eq. (S4) can be written down for the current density

at  $\omega_i, k_{ix}$  ( $i = 2, 3$ ), and we use an analogous set of conventions to indicate the fields and conductivities at other frequencies and wavevectors. In what follows, we will also adopt the more compact notation  $\sigma^{(2)}(\omega_1) = \sigma^{(2)}(\omega_1, k_{1x}; \omega_2, k_{2x}, \omega_3, k_{3x})$ , where the dependence on wavevectors and input frequencies is understood.

The substitution of Eqs. (S3) and (S4) into Eq. (S2) (along with analogous equations for the other fields  $i = 2, 3$ ) yields a set of nonlinear equations relating the transmission coefficients and incident fields,

$$t_1 = t_1^{(L)} \left[ 1 - \frac{|t_2 E_{2I}|^2}{(2c\epsilon_0)^2} t_1^{(L)} t_3^{(L)} \sigma^{(2)}(\omega_1) \sigma^{(2)}(\omega_3) \sin \phi_1 \sin^2 \phi_2 \sin \phi_3 \right]^{-1}, \quad (\text{S5})$$

$$t_2 = t_2^{(L)} \left[ 1 - \frac{|t_1 E_{1I}|^2}{(2c\epsilon_0)^2} t_2^{(L)*} t_3^{(L)*} \sigma^{(2)*}(\omega_2) \sigma^{(2)*}(\omega_3) \sin^2 \phi_1 \sin \phi_2 \sin^* \phi_3 \right]^{-1}. \quad (\text{S6})$$

Here  $t^{(L)} = \frac{2 \sin \theta}{n \sin \theta + \sin \phi + (\sigma^{(1)}/c\epsilon_0) \sin \theta \sin \phi}$  is the linear transmission coefficient, and the angle of the generated field is defined via  $k_{3x} \equiv \frac{n_3 \omega_3}{c} \cos \phi_3$ . The complex in-plane field amplitude generated at the difference frequency and at the position of the graphene layer  $z = 0$  is given by

$$E_{3x} = -\frac{t_1 t_2^* t_3^{(L)}}{2c\epsilon_0} E_{1I} E_{2I}^* \sigma^{(2)}(\omega_3) \sin \phi_1 \sin \phi_2 \sin \phi_3. \quad (\text{S7})$$

While Eqs. (S5) and (S6) may appear somewhat complicated, here we note their main features. First, we note that the input field amplitudes, the beam angles, and the linear optical properties of the system are generally known. Thus, on one hand, given a theoretical model of the nonlinear conductivity  $\sigma^{(2)}$ , these equations can be solved to obtain the predicted changes in transmission and reflection of the input beams, due to the generation of plasmons at  $\omega_3, k_{3x}$ . The plasmon field amplitude itself can be found from Eq. (S7). On the other hand, even absent a theoretical model, if changes in transmission or reflection of the incident fields are experimentally measured, one can attempt to invert these equations in order to obtain an experimentally inferred value of  $\sigma^{(2)}$ .

The description above generally holds regardless of the values of  $\omega_3, k_{3x}$ . It is particularly interesting, however, to focus on the case where they align with the plasmon dispersion relation. In the small wavevector limit and for frequencies smaller than twice the Fermi frequency,  $\omega \lesssim 2\omega_F$ , the linear conductivity is well-approximated by the Drude model [S5],

$$\sigma(\omega) \approx \frac{ie^2}{\pi\hbar} \frac{\omega_F}{\omega + i\gamma}. \quad (\text{S8})$$

Here we have included a phenomenological damping term  $\gamma$ . The plasmon dispersion relation can be found by solving for the pole of the linear transmission coefficient,  $t^{(L)}$ . For simplicity,

we will momentarily consider the case of a substrate with frequency-independent refractive index, so that the role of plasmon damping can be more clearly identified. In the absence of losses, the dispersion relation is found to be

$$k_{x,p} = \frac{(1+n^2)\omega_p^2}{4\alpha c\omega_F}, \quad (\text{S9})$$

where  $\alpha \approx 1/137$  is the fine-structure constant. In the presence of losses, choosing  $\omega_3, k_{3x}$  to lie on the plasmon dispersion relation yields a linear transmission amplitude of  $|t_3^{(L)}| \approx \frac{2nQ}{1+n^2}$ , where  $Q = \omega_3/\gamma$  is the plasmon quality factor. Under these conditions, one thus sees from Eq. (S7) that the field intensity experiences a resonant enhancement of  $|E_3|^2 \propto Q^2$ . A similar resonant effect appears in the transmission and reflection coefficients of the incident fields.

While the Eqs. (S5) and (S6) can in principle be inverted to infer  $\sigma^{(2)}$  given experimental data for reflection or transmission coefficients, in the present experimental setup this procedure can only be done semi-quantitatively due to a number of unknowns. First, the signal lies significantly above the noise floor only near the plasmon dispersion relation, and only a limited number of beam angles are investigated. This makes it difficult to infer a specific wavevector and frequency dependence of the nonlinear conductivity (fundamentally, there must be a dependence on wavevector, as otherwise  $\sigma^{(2)} = 0$  for a centrosymmetric material). Furthermore, the experiment employs pulses whose bandwidths are significantly larger than the plasmon linewidth. Given that, here we aim to reach a conservative estimate for the strength of  $\sigma^{(2)}$ , while we anticipate that future improved experiments (such as with longer pulses and nano-structures) and theoretical models will enable more detailed comparisons.

The full conductivity function at zero temperature is given by [S5]

$$\sigma(\omega) = \frac{ie^2}{\pi\hbar}\frac{\omega_F}{\omega + i\gamma} + \frac{e^2}{4\hbar} \left[ \Theta(\omega - 2\omega_F) + \frac{i}{\pi} \log \left| \frac{\omega - 2\omega_F}{\omega + 2\omega_F} \right| \right], \quad (\text{S10})$$

where  $\Theta(x)$  is the Heaviside step function. The Fermi energy  $\hbar\omega_F \approx 0.5$  eV of graphene is significantly lower than the pump and probe photon energies of  $\sim 3$  eV. At these frequencies, the linear conductivity of graphene is nearly frequency independent and real,  $\sigma^{(1)}(\omega)/(c\epsilon_0) \approx \pi\alpha$ , which we use to obtain the pump and probe linear reflection coefficients. Furthermore, we take the simplest possible function for the nonlinear conductivity,  $\sigma^{(2)}(\omega) = i|\sigma^{(2)}(\omega_2)|(\omega/\omega_2)$ , where  $|\sigma^{(2)}(\omega_2)|$  is a single fitting parameter (the probe frequency  $\omega_2$  is fixed in the experiment). With this choice of function, graphene would be equivalent to a nonlinear material with a frequency-independent bulk nonlinear susceptibility of  $\chi^{(2)} = -i\sigma^{(2)}(\omega)/(\omega\epsilon_0 t) = |\sigma^{(2)}(\omega_2)|/(\omega_2\epsilon_0 t)$ , where  $t$  is the effective thickness of

graphene. Inserting this nonlinear conductivity into Eqs. (S5), (S6), and (S7), we find that a value of  $|\sigma^{(2)}(\omega_2)| \approx 2.4 \times 10^{-12} \text{ A}\cdot\text{m/V}^2$  produces a good qualitative fit to the experimental data.

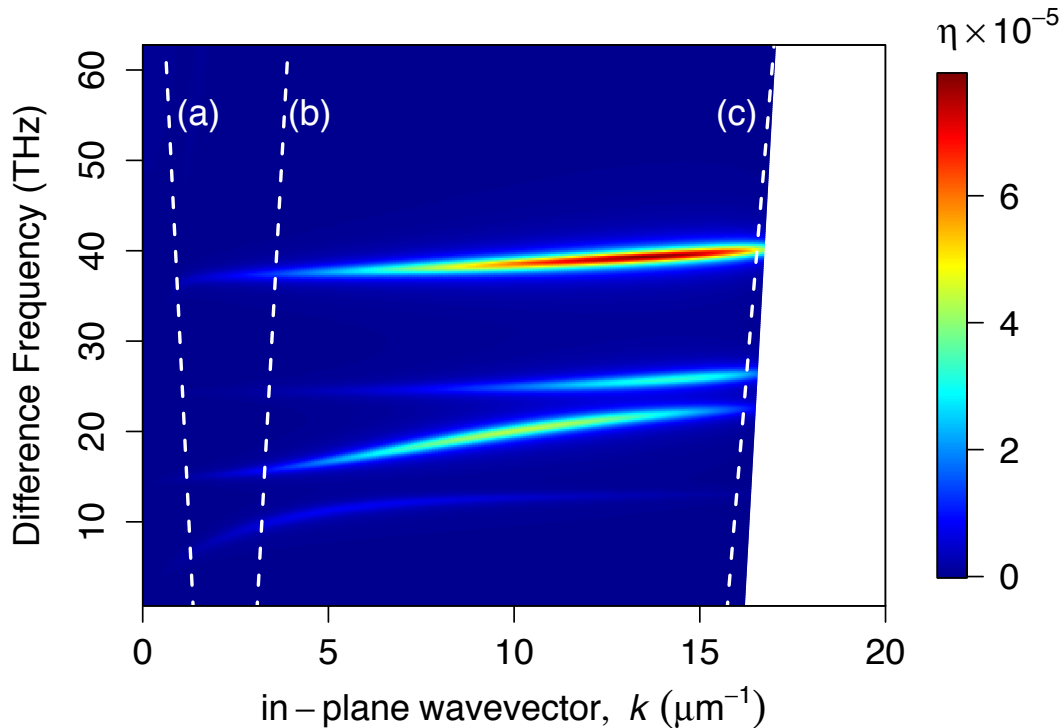


FIG. S7: The numerical solution for the pump conversion efficiency,  $\eta$ , as a function of wavevector and difference frequency.

We now discuss how to obtain the conversion efficiency of pump photons to plasmons. The number of photons dissipated per unit area and time by the field at the difference frequency consists of two terms,  $\Gamma_d = \Gamma_{d,g} + \Gamma_{d,s}$ . The first term consists of damping from the graphene layer due to the real part of its conductivity, and is given by  $\Gamma_{d,g} = (\text{Re } \sigma^{(1)}(\omega_3)) |E_{3x}|^2 / (2\hbar\omega_3)$ . The second term is due to damping from the substrate, due to the fact that at low frequencies its refractive index is complex. This contribution is given by  $\Gamma_{d,s} = \frac{\epsilon_0}{4\hbar|\text{Im}(k_{3x} \tan \phi_3)|} (\text{Im } n^2(\omega_3)) |E_{3x}|^2 (1 + |\cot \phi_3|^2)$ . On the other hand, the incident photon flux in the pump field is  $\Gamma_{\text{in}} = I_1 \sin \theta_1 / (\hbar\omega_1)$ , where  $I_1$  is the pump intensity. Generally, the amplitude of the generated plasmon field rate will depend on both the pump and probe intensities. However, at the level of individual photons, the process is that an

incoming pump photon gets converted to a plasmon (assisted by stimulated emission of a photon into the probe). Thus, we define the conversion efficiency relative to the pump alone. In steady state, the rates of photons dissipated and generated at the difference frequency are equal, and thus the overall conversion efficiency of pump photons to plasmons is  $\eta = \Gamma_d/\Gamma_{\text{in}}$ . This efficiency is shown in fig. S7 for the range of frequencies and wavevectors used in our experiments. Using the estimated value of  $|\sigma^{(2)}(\omega_2)|$ , we find that the conversion efficiency for the experimental arrangement shown in fig. 3(b) at the point of maximum signal is approximately  $\eta \approx 6 \times 10^{-6}$  for the experimental intensities used.

### Substrate Response

Differential reflection was recorded as a function of delay time for both the graphene on quartz and for the bare quartz substrate to ascertain any contribution to the nonlinear response from the substrate. The experimental parameters for these data were set to the resonant condition of figure 3(b), with  $\theta_{\text{pump}} = 50^\circ$ ,  $\theta_{\text{probe}} = 70^\circ$  and the difference frequency set to 10 THz. The measurements are compared in figure S8, and negligible signal, compared to the resonant measurement from graphene, is observed.

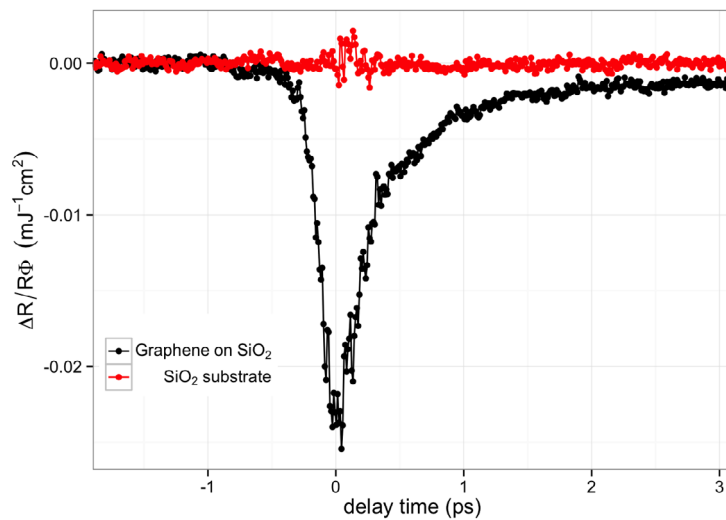


FIG. S8: Differential reflection normalized to fluence as a function of temporal overlap for: Graphene on quartz (black) and the bare quartz substrate (red) at  $\theta_{\text{pump}} = 50^\circ$ ,  $\theta_{\text{probe}} = 70^\circ$ .

- [S1] Hale, P. J., Hornett, S. M., Moger, J., Horsell, D. W. & Hendry, E. Hot phonon decay in supported and suspended exfoliated graphene. *Phys. Rev. B* **83**, 121404 (2011).
- [S2] Tielrooij, K. J. *et al.* Photoexcitation cascade and multiple hot carrier generation in graphene. *Nature Physics* **9**, 248–252 (2013).
- [S3] Luxmoore, I. J. *et al.* Strong Coupling in the Far-Infrared between Graphene Plasmons and the Surface Optical Phonons of Silicon Dioxide. *ACS Photonics* **1**, 1151–1155 (2014).
- [S4] Kitamura, R., Pilon, L. & Jonasz, M. Optical constants of silica glass from extreme ultraviolet to far infrared at near room temperature. *Applied Optics* **46**, 8118–8133 (2007).
- [S5] Wunsch, B., Stauber, T., Sols, F. & Guinea, F. Dynamical polarization of graphene at finite doping. *New Journal of Physics* **8**, 318 (2006).